rium polymeric units in most igneous melts will be determined by disproportionation reactions 2 and 3.

D. VIRGO
B. O. MYSEN
I. KUSHIRO

Geophysical Laboratory, Carnegie Institution of Washington, Washington, D.C. 20008

References and Notes

1. P. C. Hess, *Geochim. Cosmochim. Acta* **35**, 289 (1971); C. R. Masson, *Proc. R. Soc. London Ser. A* **287**, 201 (1965).
2. C. W. Lentz, *Inorg. Chem.* **3**, 574 (1964); C. R. Masson, *J. Non-Cryst. Solids* **25**, 3 (1977); R. M. Smart and E. P. Glasser, *Phys. Chem. Glasses* **19**, 95 (1978).
3. L. S. Dent Glasser, *Z. Kristallogr.* **149**, 291 (1979).
4. S. A. Brawer and W. B. White, *J. Chem. Phys.* **63**, 2421 (1975).
5. W. L. Konijnendiijk, *Philips Res. Rep. Suppl.* 1 (1977).
6. H. Verweij, *J. Non-Cryst. Solids* **33**, 41 (1979); *ibid.*, p. 51.
7. J. R. Sweet and W. B. White, *Phys. Chem. Glasses* **10**, 246 (1969).
8. S. K. Sharma, D. Virgo, B. O. Mysen, *Carnegie Inst. Washington Yearb.* **77**, 649 (1978).
9. A. N. Lazarev, *Vibrational Spectra and Structures of Silicates* (Consultants Bureau, New York, 1964).
10. S. A. Brawer, *Phys. Rev. B* **11**, 3173 (1975).
11. F. L. Galeaner, *ibid.* **19**, 4292 (1979); P. N. Sen and M. F. Thorpe, *ibid.* **15**, 4030 (1977).
12. D. M. Adams and I. R. Gardner, *J. Chem. Soc. Dalton Trans.* **1974**, 1502 (1974); *ibid.* **1976**, 315 (1976).
13. R. J. Bell and P. Dean, in *International Conference on the Physics of Noncrystalline Solids, 3rd, University of Sheffield, 1970*, R. W. Douglas and B. Ellis, Eds. (Wiley-Interscience, London, 1972), pp. 443–452.
14. The Raman spectra were taken on small chips of glass (~0.5 mm). Experimental details are similar to those given by Sharma *et al.* (*8*).
15. The starting mixes were prepared from spectrographically pure oxides that were thoroughly mixed, melted, and quenched in molybdenum disilicate-wound vertical quench furnaces. For melt compositions along the Ca_2SiO_4–SiO_2 and $CaMgSiO_4$–SiO_2 joins, the oxide mixes were held at 1650°C for 1/2 hour in sealed platinum capsules. The capsules were quenched in water at a rate of about 500°C per second.
16. D. Virgo, F. Seifert, B. O. Mysen, *Carnegie Inst. Washington Yearb.* **78**, 502 (1979).
17. M. Taylor, G. E. Brown, P. H. Fenn, *Geochim. Cosmochim. Acta*, in press.
18. B. O. Mysen, F. Seifert, D. Virgo, *Am. Mineral.*, in press; B. O. Mysen, R. Ryerson, D. Virgo, *ibid.*, in press.

27 March 1980

Spaceborne Imaging Radar: Monitoring of Ocean Waves

Abstract. *A well-organized, very low energy ocean swell system off the East Coast of the United States was tracked with the Seasat synthetic aperture radar from deep water, across the continental shelf, and into shallow water. The results indicate that spaceborne imaging radar may be used to accurately measure ocean wavelength and direction, even in coastal areas and in the presence of a mixed ocean.*

A number of aircraft studies in the past few years have indicated that ocean swell can be imaged with synthetic aperture radar (SAR), at least for some values of wind velocity when there is a substantial component of the swell traveling along the line of sight of the radar (*1*). The bounds of wind, wave, and geometric conditions over which reliable ocean wave detection occurs, however, remain elusive for want of an extensive experimental data base. Seasat provided a unique, although limited, opportunity to reexamine the wave detection problem without some of the artificial constraints of aircraft measurements. A concise summary of the Seasat SAR design parameters and a more general description of the total Seasat SAR system and some of its fundamental information limitations have been given in (*2*). A preliminary assessment of the Seasat SAR ocean wave detection capabilities has been compiled in (*3*).

During the limited 100-day lifetime of the Seasat SAR, data from more than 400 passes of duration ranging from 1 to 15 minutes were collected at three domestic and two foreign receiving stations. About 20 of these passes provided acceptable SAR imagery within 70 km of a well-instrumented "sea truth" pier operated by the U.S. Army Corps of Engineers, Coastal Engineering Research Center (CERC) at Duck, North Carolina. The Applied Physics Laboratory of the Johns Hopkins University, along with several government agencies, collected a variety of wind and wave measurements during a concentrated 8-week period from 12 August to 9 October 1978.

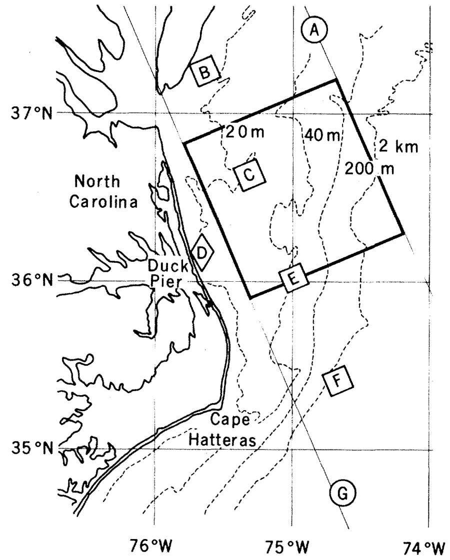

On the morning of 28 September 1978, at 1520 G.M.T., Seasat approached the East Coast of the United States, with the SAR 100-km swath running approximately parallel to the coast but displaced eastward by about 20 km. On the basis of the present analysis of that pass, several major conclusions may be reached:

1) The SAR can successfully detect low-energy swell systems of significant wave heights, H_s, well under 1 m (actually 0.65 ± 0.25 m), at least for surface windspeeds (normalized to 10 m above sea level) of 2 m/sec $\leqq U_{10} \leqq$ 10 m/sec.

2) Refraction of low-energy but well-organized swell due to local changes in ocean depth is clearly detectable in wavelength.

3) The complexity of the ocean spectrum (for example, whether it is composed of more than one system or is spread in direction and wave number) seems to have little bearing on the threshold detection limits.

Figure 1 identifies the various regions off the East Coast for which estimates or measurements of wind and waves were collected on the morning of 28 September. For reference, the edges of the 100-km SAR swath are shown by the solid lines inclined at approximately 23° with respect to north at this latitude. The locations are keyed in alphabetical order from north to south. Location A corresponds to the Navy Fleet Numerical Weather Central (FNWC) grid point 271. Locations B, C, E, and F are areas, each 15 km square, over which the Seasat SAR imagery was optically Fourier-transformed. The local ocean depth (shown with dashed contours in Fig. 1) changes appreciably over the 15-km square at locations B, C, and E, which would cause appreciable spreading of a single-frequency, deep-water wave in both wavelength and direction. Deep-water dispersion prevails only at location F for wavelengths greater than 70 m. Local depth changes at location B are especially severe, ranging from less than 10 m to at least 20 m. The National Oceanic and Atmospheric Administration (NOAA) Sea Air Interaction Laboratory aircraft laser profilometer was operating at location E. In situ, one-dimensional spectral measurements were collected at the CERC pier (location D). The FNWC grid point 260 is represented by location

Fig. 1. Locations of surface, aircraft, and spacecraft measurements of the low-energy swell systems present on 28 September 1978. The cover image is located by the 100-km square centered at 36.5°N and 75.1°W.

0036-8075/80/0620-1373$00.50/0

G and provides a convenient reference spectrum for the SAR imagery collected at location F. Locations F and G are the only deep-water locations of Fig. 1.

Time histories of the long (> 1-second) waves were recorded by five separate instruments in the vicinity of the research pier for a 20-minute interval spanning the satellite overpass time. The one-dimensional, long-wave spectrum was measured in the vicinity of the research pier with two Baylor gauges, two wave rider buoys, and one capacitive wave staff. Spectra from each instrument showed varying amounts of 11-second and 7-second systems. The average of the two gauges and the two buoys was calculated and clearly identified each wave system. The H_s derived from the averaged spectrum was 1.0 m, which includes the combined energy from both the 11-second and 7-second systems. The H_s corresponding to each of the two systems separately (being roughly equal in energy at the pier) is closer to 0.7 m. By comparison, the FNWC grid point closest to the pier (location G of Fig. 1) yields an H_s estimate of 0.4 m for the long-wave system and 0.6 m for the short-wave system.

The NOAA aircraft laser spectrum (courtesy of D. Ross of the NOAA Sea Air Interaction Laboratory) verified a double wave system having predominant periods of 11 seconds and 7 seconds, and total H_s equal to 1.26 m or approximately 0.9 m for each system. The energy of the 7-second system is probably underestimated because of the directional sensitivity of the laser profilometer. The energy of the 11-second system, however, should be accurately indicated and probably represents an effective upper bound to the H_s in the transformed areas. The NOAA aircraft measured surface winds U_{10} up to 10 m/sec south of location F and down to 2 m/sec between locations C and E.

In summary, then, three separate measures of the 11-second system yielded a range of H_s of 0.4 m $< H_s <$ 0.9 m, the lower bound from FNWC and the upper bound from the NOAA aircraft laser profilometer. The average of the four CERC pier measurements yielded an H_s of 0.7 m for the 11-second system.

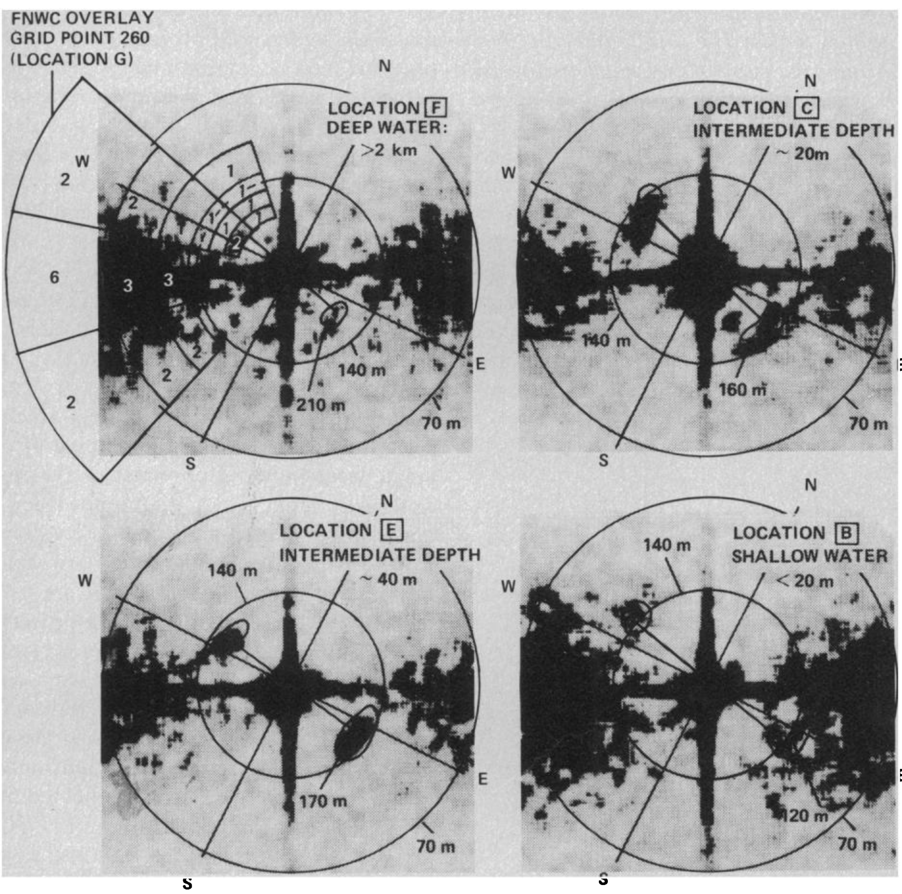

Fig. 2. Optically processed, optically transformed, and digitally enhanced SAR wave spectra from locations F, E, C, and B shown in Fig. 1. The sequence moves from deep to shallow water and illustrates both wavelength and direction change as the 11-second swell system approaches shore. The overlay of the FNWC spectra for grid point 260 (location G) on the SAR image spectrum at location F shows remarkable correlation of the longer wavelength swell system present on 28 September. Units in the overlay are relative energy units per cell.

The spacecraft SAR was activated for approximately 4 minutes on 28 September as it approached the East Coast. The radar operating wavelength is approximately 23 cm, and for the Seasat geometry the image intensity (or reflected power) is generally proportional to the amplitude of Bragg scatterers of 30- to 40-cm wavelength on the ocean surface (*4*). The amplitude of the scatterers may be strongly (but not solely) correlated with surface wind at the air-sea boundary. The image displayed on the cover, for example, illustrates the presence of a variety of surface-scattering mechanisms, some of which bear only an indirect relationship to the surface wind. In general, however, brighter regions of the image correspond to higher winds and darker regions to lower winds. The large dark area in the center of the cover corresponds to a region of very low winds (< 2 m/sec). The location of the cover image is designated by the square in Fig. 1.

Spacecraft SAR imagery was optically Fourier-transformed, digitally scanned at the equivalent of 6-m ground resolution, spatially averaged by means of a sliding window (7 by 7 elements), and contrast-enhanced with a three-segment, piecewise-linear level transformation with a very high center segment gain. Each set of breakpoints was individually optimized to compensate for the variations in average intensity.

Figure 2 shows a progression of enhanced optical Fourier transforms representing the image spectra at locations F, E, C, and B as the wave trains approach shore. The sequence shows the refraction effects of the variations in ocean depth on the long-wave component. An ocean wave 210 m long at location F shortens to 170 m at location E, 160 m at location C, and 120 m at location B in shallow water. Furthermore, the deep-water spectrum F correlates well with the FNWC estimate of spectral peaks in both wave number and direction taken from location G (grid point 260).

The presence of a short-wave system is also evident on the transforms. This short-wave energy correlation may be at least in part an artifact of the JPL optically correlated and transformed imagery. More recent digitally processed and transformed imagery of the same area shows much weaker correlations in the short-wave (7s) portions of the spectrum.

No correlation between spectral energy density and image transform density has been attempted. A proper treatment of this question would require careful accounting of the many system nonlinearities, some deliberately introduced for enhancement and some unknown. A better understanding of oceanic backscatter models (*1*, *4*) is also a prerequisite for further progress here.

An overall comparison of all available measures of wave frequency (by wavelength and bathymetry) and direction for 28 September yields a variance between measurements of the same order as the confidence in a particular measurement. For the data set presented here, the SAR measured ocean wavelength and direction as well as any of the alternate techniques available. It is possible that, for separating swell systems in a mixed ocean, its accuracy may exceed that of any other existing technique.

ROBERT C. BEAL

Applied Physics Laboratory,
Johns Hopkins University,
Laurel, Maryland 20810

References and Notes

1. W. E. Brown, Jr., C. Elachi, T. W. Thompson, *J. Geophys. Res.* **81**, 2655 (1976); C. Elachi, *ibid.*, p. 2657; _____ and W. E. Brown, *IEEE Trans. Antennas Propag.* **AP-25**, 84 (1977); R. A. Shuchman, E. S. Kasischke, A. Klooster, "Synthetic Aperture Radar Ocean Wave Studies" (Final Report 131700-3-F, Environmental Research Institute of Michigan, Ann Arbor, 1978); P. G. Teleki, R. A. Shuchman, W. E. Brown, Jr., W. McLeish, D. B. Ross, M. Mattie, paper presented at the Oceans '78 Conference, Washington, D.C., 1978.
2. R. Jordan, paper presented at the Synthetic Aperture Radar Technical Conference, Las Cruces, N.M., 1978); R. C. Beal, in *29th International Astronautical Federation Congress Proceedings* (Pergamon, New York, in press).
3. F. I. Gonzalez *et al.*, *Science* **204**, 1418 (1979).
4. J. W. Wright, *IEEE Trans. Antennas Propag.* **AP-16**, 217 (1968).
5. This work was jointly supported by the National Oceanic and Atmospheric Administration and the National Aeronautics and Space Administration as a portion of the Seasat Announcement of Opportunity Program under contract MO-A01-78-00-4330. The digitally processed and color-enhanced image of the ocean displayed on the cover was provided by C. Wu of the Jet Propulsion Laboratory. I thank J. Dunne and W. Brown of the Jet Propulsion Laboratory for providing Seasat data.

1 October 1979; revised 11 January 1980

Arctic Steppe-Tundra: A Yukon Perspective

Abstract. *The first reliable, securely dated full- and late-glacial pollen stratigraphy from Eastern Beringia forces the rejection of the widely held hypothesis of a steppe-tundra or grassland associated with extinct vertebrates and early humans. The arctic-alpine fossil flora and low pollen influx suggest a sparse tundra similar to modern herb fell-field vegetation.*

Beringia was a land bridge for plants, animals, and people between Siberia and North America (*1*). The northern Yukon and adjacent Alaska, commonly referred to as Eastern Beringia, were isolated from the rest of North America by the maximum extensions of Late Quaternary ice sheets (*2*), and recent discoveries suggest that the area was a full-glacial refugium for a varied fauna, now mostly extinct, and for humans (*3*, *4*). The assumption is widely held that the apparently rich, largely herbivorous fauna of extinct horse, bison, mammoth, camel, and saiga antelope was supported by an arctic steppe or grassland. Since the work of Livingstone (*5*), pollen data from the few sites in Alaska that have been investigated show an herb assemblage dominated by grass, sage, and sedge, widely regarded as registering this "extinct biome." Our results do not support a steppe or grassland interpretation for the period between 30,000 and 14,000 years before present (B.P.).

We report here late Pleistocene pollen records from two lake sites (*6*). Both lie just outside the western limit of Wisconsinan glaciation (*7*) and are 275 km apart. Hanging Lake is in the tundra on rolling plains, and Lateral Pond is within forested mountains, so they are representative of easternmost Beringia.

Hanging Lake (informal name) is 500 m above sea level in shale and sandstone on an undulating tundra surface 35 km northeast of the edge of the Old Crow Flats (Fig. 1). It has a surface area of about 60 ha and a maximum water depth of 9.5 m. There is no inlet stream, and a single small outlet occurs at the northeastern end. White spruce (*Picea glauca*) occurs in an outlying stand 30 km west-northwest of the lake. There are four main types of vegetation: (i) extensive cotton grass (*Eriophorum vaginatum*) tussock tundra on flat and gently sloping surfaces; (ii) local sedge (*Carex*) meadow on poorly drained sites; (iii) heath tundra with *Empetrum*, *Vaccinium vitis-idaea*, *Arctostaphylos alpina*, *Betula glandulosa*, and lichens on upland granular soils; and (iv) species-rich discontinuous tundra or fell-field vegetation on widespread rocky surfaces of exposed upland sites.

The percentages (Fig. 2) show that the pollen stratigraphy conforms to the pattern typical for Eastern Beringia. The basal herb zone (30,000 to 14,000 years B.P.), dominated by *Artemisia*, Gramineae, and Cyperaceae, is replaced by a rapid increase in birch, then spruce, and finally alder. The high percentages of *Artemisia* and Gramineae are usually cited as the main evidence for the steppe or grassland interpretation. The influxes of these herb pollen types (Fig. 2), however, as calculated from close-interval radiocarbon dates (*8*), are equal to their Holocene values; this result suggests that these herb types were no more abundant in the past than they are today. Furthermore, the herb and total pollen influxes are lower during the herb zone than at any subsequent time. Of the major herb types, only Cruciferae, Chenopodiaceae/Amaranthaceae, *Plantago canescens*, and Tubuliflorae (the latter two not shown in Fig. 2) have maximum influxes in the herb zone, but at very low values of less than 5 grain cm^{-2} $year^{-1}$. The influx of birch within the herb zone is negligible despite percentages of up to 30. The influx data thus show that the vegetation must have been sparser and herbs less abundant in arctic steppe-tundra than at present.

The floristic affinities of the herb zone are clearly arctic-alpine and not cold-temperate grassland. These include *Aconitum*, *Bupleurum triradiatum*, Caryophyllaceae, *Dryas*, *Astragalus*, *Oxytropis*, *Hedysarum*, *Androsace*, *Lesquerella arctica*, *Pedicularis*, *Phlox*, *Polemonium*, *Polygonum alaskanum*, *P. viviparum*, *Oxyria*, *Rumex*, *Saxifraga hi-*

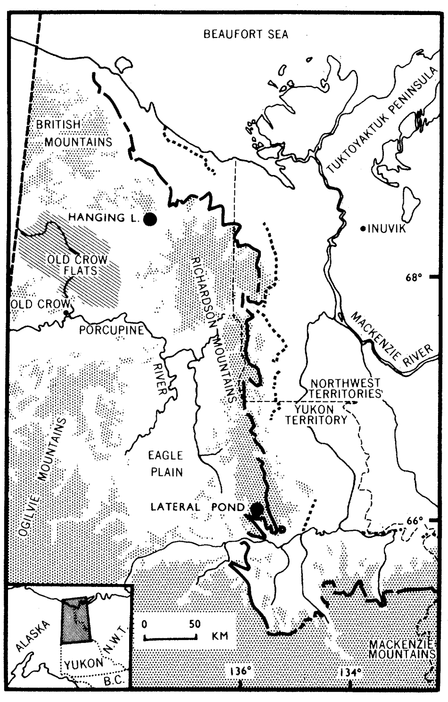

Fig. 1. A sketch map of the northern Yukon and adjacent Northwest Territories, showing the locations of Hanging Lake and Lateral Pond. The heavy dotted line indicates the maximum westernmost extent of Wisconsinan glaciers. The heavy dashed line marks the maximum westernmost extent of the penultimate glaciation.

0036-8075/80/0620-1375$00.50/0